Ultrafast phase transitions in polyamorphic materials triggered by swift heavy ion impacts

Henrique Vázquez ● and Flyura Djurabekova[*]

Helsinki Institute of Physics and Department of Physics, University of Helsinki, 00014 Helsinki, Finland

We report unexpectedly fast phase transitions inside the track as pressure and temperature develop after a swift heavy ion impact. By means of molecular dynamics simulations we reveal the origin of the core-shell fine structure observed in a-SiO$_2$ and a-Si$_3$N$_4$, as well as the dense core in a-Si. The fine structure of the track is composed of two distinct amorphous phases that result from the different pressure levels in the core and in the shell during solidification. We link this behavior to the tetrahedral network present in these materials.

I. INTRODUCTION

Swift heavy ions (SHIs) deposit large amounts of energy via inelastic scattering with electrons as they travel through a solid material. The intense excitation translates into strong heating along the ion path and can produce permanent cylindrical structural modifications in the material, known as ion tracks.

It has been repeatedly seen in experiments that swift heavy ions (SHI) form tracks with distinct core-shell structure in silica (a-SiO$_2$) and amorphous silicon nitride (a-Si$_3$N$_4$) [1–4]. Atomistic simulations corroborated these findings, furthermore showing that tracks in a-SiO$_2$ and a-Si$_3$N$_4$ have underdense cores surrounded by the overdense shells [1,3,5]. This fine structure of the tracks, however, has not been observed in all amorphous materials. The measurements of the tracks in amorphous silicon (a-Si) showed only an overdense core [6] and in amorphous carbon [7] and in some metallic glasses the density within the tracks was found to be lower than in the surrounding matrix [8,9].

The reason behind the different response of amorphous materials to SHI irradiation has not been yet clarified. A few hypotheses were suggested to explain the mechanisms. For instance, the formation of a densified shell has been attributed to viscous flow of molten phase into surrounding solid matrix, while the low-density core has been explained by the fast quenching of the disordered material in the center of the track [3,5,10]. In Ref. [11], the overdensification within the track was explained by the density anomaly found in a-SiO$_2$ at high temperatures in the molten phase. If frozen, such denser state may remain in the matrix even after it was cooled to room temperature. This mechanism, however, does not explain the formation of the underdense track core, which was found to be a prominent feature of ion tracks in this material in many studies, including [1].

On the other hand, materials, such as a-SiO$_2$ and a-Si, have been found to exhibit polyamorphism [12], i.e., the ability to exist in more than one amorphous phase. These materials are able to reorganize their tetrahedral networks or even increase coordination of Si atoms under applied pressure. For instance,

a-SiO$_2$ is able to undergo continuous structural modifications with increasing pressure. It was shown that at high temperatures irreversible densification of a-SiO$_2$ structure may take place already at 3–5 GPa [13]. In this pressure regime, the structural modifications appear only in the long-range order, changing the topology of the network. Similar densification of the molten phase was reported in other silicates as well [14].

Amorphous silicon can also be found in several amorphous phases depending on the pressure. Moreover, two liquid phases, the low-density liquid (LDL) and the high-density liquid (HDL) were also recently reported for silicon [15–17]. Polyamorphism of a-Si$_3$N$_4$ is studied to lesser extent, although its structure is based on tetrahedral network that is often linked to polyamorphism.

The necessary conditions for a polyamorphic phase transformations may be created in these materials during the impact of a SHI. The energy deposited by the SHI generates localized high pressures and temperatures that may lead to polyamorphic structural changes in the regions inside the ion track.

In our work, we follow the transient states of temperature and pressure within the track region to explore the role of pressure on ultrafast phase transitions that take place inside the track. We find a remarkable correlation between these structural modifications and the core-shell structures observed experimentally.

II. METHODS

We simulate the SHI impacts in a-SiO$_2$, a-Si$_3$N$_4$, and a-Si materials by means of molecular dynamics (MD) simulations. To describe the interatomic interactions, we apply a range of interatomic potentials available for the studied materials. We simulate a-SiO$_2$ with the Munetoh (Mu) [18] and Watanabe-Samela (WS) [19] potentials and a-Si$_3$N$_4$ with the Mota potential [20]. For a-Si we employ three different potentials: Tersoff (T) [21], Stillinger-Weber (SW) [22], and a machine-learning Gaussian approximation potential (GAP) trained with Si DFT data [23]. These potentials have been previously employed to study the behavior of these materials at equilibrium conditions [24–27], and under ion irradiation in both nuclear and electronic stopping power regimes [3,4,6,28–37].

---

[*]flyura.djurabekova@helsinki.fi

For our simulations, we mainly use the classical MD code PARCAS [38] and only for the simulations with the GAP potential, we use the LAMMPS MD code [39]. The amorphous structures were obtained either with the quench-from-melt method (a-Si$_3$N$_4$ and a-SiO$_2$ (M)) as in Ref. [3] or with the Wooten-Winer-Weaire (WWW) Monte Carlo method [40] followed by annealing runs at elevated temperatures—SiO$_2$ (WS), Si (T, SW, and GAP)—as in Ref. [41]. In the main text we only show the results corresponding to the Watanabe-Samela, Mota and GAP potentials. We include analogous analysis for the other potentials in the Supplemental Material [42].

SHIs deposit the energy in materials via electronic excitations; this energy is subsequently transferred to the atoms via the electron-phonon coupling mechanism. We model this process in SiO$_2$ and Si$_3$N$_4$ using the two-temperature model (TTM) [43] with the source function given by the Waligorski distribution [44]. In silicon, the carrier multiplication is much stronger, hence, in this material we described the carrier dynamics and the energy transfer to the lattice by the Monte Carlo two-temperature model (MC-TTM) similarly as it was done in Refs. [6,45]. We also note that we used the instantaneous energy deposition scheme to simulate the SHI ion impacts in SiO$_2$ and Si$_3$N$_4$, whereas the energy in a-Si was introduced according to the energy transfer rate in MC-TTM.

The energy is deposited by assigning the corresponding velocities in random directions to the atoms within the track. We applied a thermostat at the lateral borders of the cell to emulate the cooling effect of the surrounding cold amorphous matrix. We use the same Au ion with the energy of 185 MeV and the same TTM parameters as in Refs. [3,6], since the simulation results with this parametrization were found to be in a good agreement with experiment. Thermodynamic properties, such as temperature and pressure, are vaguely defined in the length and time scales of ion track formation. We obtain statistically meaningful values of temperature (T^*) and pressure (P^*) inside the track by averaging these quantities within nanometer-thick cylindrical shells comprising ∼10000 atoms (1000 atoms in the simulations with GAP) coaxial with the ion track. The hydrostatic atomic pressure was also averaged over the time intervals of either 100 or 300 fs and was obtained from the per-atom virial stress-tensor including the kinetic component.

The irradiation simulations were performed with simulation cells of approximate dimensions $25 \times 25 \times 50$ nm^3. We tested the convergence with cell size by using a cell twice as large in the lateral dimensions for a-SiO$_2$ with the Watanabe potential, and we observed the same density profile as in the smaller cell (for more information, see the Supplemental Material [42]). Due to the large computational cost of the bigger cells, we decided to perform the rest of the simulations with the cell of the original dimensions.

III. RESULTS

A. Dynamics of density modulation during ion track formation

In Fig. 1, we show the spatiotemporal evolution of densities in all three materials after the initial deposition of energy. The graphs show representative results for a-SiO$_2$ in the Watanabe
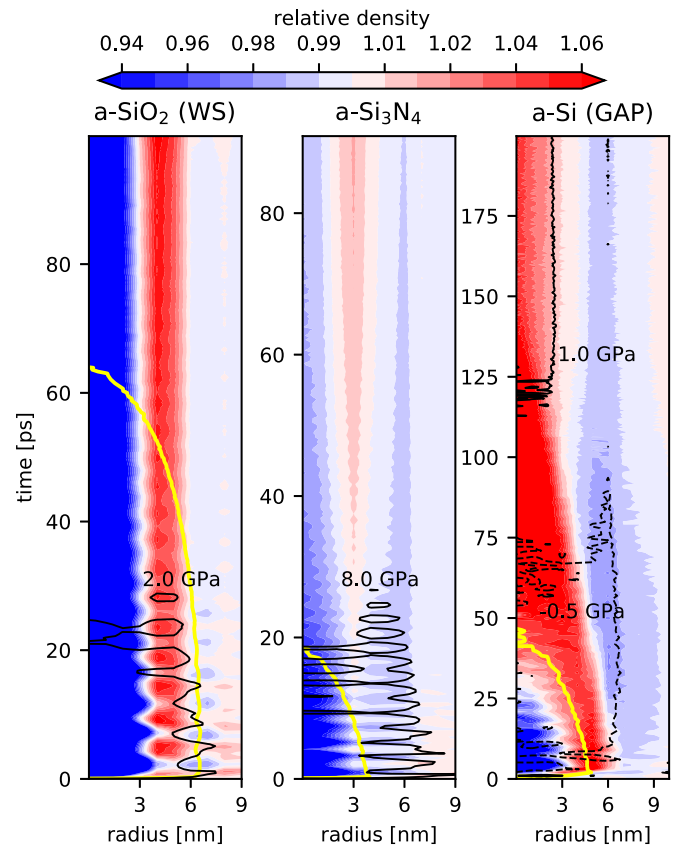

FIG. 1. Time evolution of the radial density after the impact of Au 185 MeV ion in three materials: a-SiO$_2$ (left), a-Si$_3$N$_4$ (center), and a-Si (right). The color shows spatiotemporal radial distribution of the relative density change away from the ion path (at the beginning of the horizontal axis). The figures from the bottom to the top (the vertical axis) show the dynamic of radial distribution of the density change from the instant right after the impact and until the track has cooled down. The density change is averaged along the z axis within the concentric cylindrical shells from the ion path. The range of density changes is given by the color scale bar at the top of the figure. The solid yellow lines illustrate the propagation of the melting/solidification front and the black lines are the isobaric contours for some reference pressure values.

potential, for a-Si$_3$N$_4$ in the Mota potential and for a-Si in the GAP potential. The other potentials predicted similar evolution dynamics; the corresponding figures can be found in the Supplemental Material online [42]. The graphs show that shortly after the ion impact the underdense core and overdense shell start developing in a-SiO$_2$ and a-Si$_3$N$_4$. The formed fine structure remains until the end of the simulation. In a-Si, on contrary, the initially underdense core turns overdense within the first 50 ps of track evolution and remains densified until the end of the simulation. These results are consistent with experimental observations as well as with previous simulation results [3,6].

The isothermal contours shown in yellow in Fig. 1 outline the regions where the temperature reached above the melting point in the respective MD potential. These regions shrink with time, however, we see that overdensification takes place where the temperature stays above the melting point for
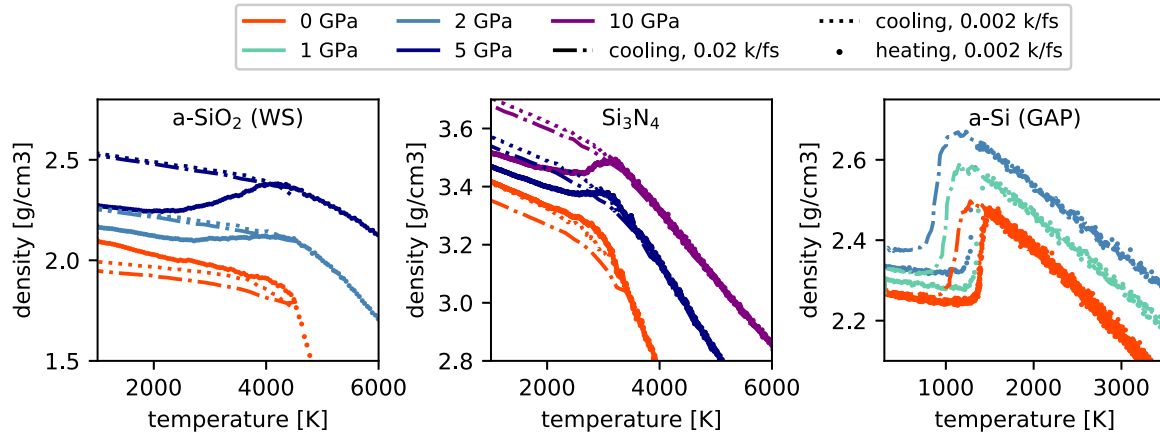
FIG. 2. Density evolution during a heating/cooling cycle at different pressures in a-SiO$_2$ (WS) with Watanabe-Samela, a-Si$_3$N$_4$ and a-Si (GAP). We show the heating data (also referred as $\rho^{q\text{EOS}}(T, P)$ in the text) with points, and the cooling data for 0.002 K/fs and 0.02 K/fs with dotted and dashed lines, respectively.

several picoseconds. Due to the rapid thermal expansion in the track core, we also register high pressure inside of the simulation cells. Black isobaric contours outline the regions where the pressure exceeds ∼8 GPa in a-Si$_3$N$_4$ and ∼2 GPa in a-SiO$_2$. We see that the track in these materials solidifies under elevated pressure.

In silicon, on contrary, the high density of a liquid phase gives rise to tensile stresses inside the track at the early stages of the track development. As the track starts cooling down, the liquid silicon within the track undergoes a phase transition from HDL to LDL and the pressure rapidly rises to 1–2 GPa during the core solidification. In the three materials, the pressure remains high for tens of picoseconds and, hence, providing sufficient condition to trigger polyamorphic phase transitions in the cell.

Since we focus our study on ultrafast phase transitions during development of an ion track, we note that we do not aim to reproduce the density differences in the core-shell structure of the track to match exactly those that were measured in experiment. First, the experimental values are given by averaging over the large number of tracks in the structures irradiated to relatively high fluences. Second, the long-term relaxation processes may modify somewhat the density changes seen within the short time span of MD simulations. The long-term relaxation may play an important role in the analysis of the density differences in a-SiO$_2$, which is able to undergo partial relaxation of built-in stresses at relatively low temperatures [46,47]. In Ref. [48], it was shown that the interatomic potentials, that are also chosen for the present study, capture correctly the fine structure of the tracks in both materials, SiO$_2$ and Si$_3$N$_4$, offering an opportunity to investigate in detail the atomic dynamics of these very fast phase transitions.

B. Pressure effect on density in amorphous structures

We complement the study of the dynamics inside the ion track with near-to-equilibrium simulations of phase transitions at elevated hydrostatic pressures and temperatures in the same materials. We investigate how the pressure and cooling rates affect the density of the structures. For these simulations we use smaller cells of approximately 5000 atoms. The

temperature and pressure are controlled everywhere in the cell by the thermo- and barostats according to the Berendsen algorithms [49], while the Nosé-Hoover approach [50] is used in the simulations with the GAP potential.

It is clear that the true equation of state (EOS) for a given material cannot be achieved within the time and length scale of MD simulations. However, since the initial structures of the studied materials were thoroughly optimized within the respective potentials, the heating curves obtained by slowly heating the amorphous network at fixed pressure values in the NPT ensemble are sufficiently close to the true EOS at those pressure and temperature values for the purpose of the given study. For clarity we will refer to these simulations as corresponding to quasiequilibrium EOS (qEOS).

In Fig. 2 we show the variation of quasiequilibrium density $\rho^{q\text{EOS}}(T, P)$ as a function of temperature in all three structures heated under different pressures with the rate of 0.002 K/fs. After the temperature in the system reaches far above the melting point, we cool the structures slowly with the same rate of 0.002 K/fs. In the same graphs, we plot the evolution of the density upon cooling with the faster rate of 0.02 K/fs. This rate reduces the temperature in the system by 2000 K in 100 ps, which is comparable to the typical cooling rates inside of an ion track. Due to the computational costs of simulations with GAP, we performed only fast rate (0.02 K/fs) heating and cooling of the system in this potential.

Figure 2 shows that at zero pressure both a-Si$_3$N$_4$ and a-Si recover the original density during slow cooling. We note that a-Si recovers the original density in GAP even with the fast cooling rate. The Stillinger-Weber and Tersoff potentials (see Supplemental Material [42]), showed densification of the a-Si structures with the faster cooling rate.

We notice that the density of the liquid phase of a-SiO$_2$ in the Watanabe potential tends towards underdensification even with the slow cooling rate. Moreover, neither Watanabe, nor Munetoh potentials (see Supplemental Material [42]) predict the density anomaly during the solid-to-liquid phase transition in a-SiO$_2$ [46]. This anomaly was previously reproduced with the BKS potential [51]. However, in the present study, we do not aim to analyze the long-range electrostatic interactions, which may affect slight compactification seen in a-SiO$_2$ upon

melting, but rather the way covalent bonds can reorganize under elevated pressures and temperatures. The latter is not accessible in the BKS potential, but is crucial for the studied transitions.

The curves showing the density evolution during the heating under applied hydrostatic pressure show densification of the molten phase in all three materials. Densification of the molten phase of a-SiO$_2$ was reported in Ref. [14], which was linked to the rearrangement of the tetrahedral network of SiO$_4$ tetrahedra. Moreover, we notice that if the material in the densified liquid phase solidifies under pressure, the amorphous network remains compactified. In a-SiO$_2$ and a-Si$_3$N$_4$ the densification shows no dependence on the cooling rate either (compare the dotted and dash-dotted lines in Fig. 2).

Furthermore, we analyze how the structures densified under pressure, relax once the pressure is removed while kept at constant temperature. With this purpose, starting from the densified structures at pressure P_1, we run additional NPT simulations where the pressure is relaxed to a lower value P_2. We compare the remaining densification at the end of the simulation to the density, which the structure should have according to the qEOS at the pressure P_2 and the same temperature [$\rho^{qEOS}(P_2, T)$ in Fig. 2]. In other words, we follow the density relaxation process through the value of the excess density during the relaxation run $P_1 \rightarrow P_2$, which is defined as

$$\delta\rho_{P_1 \rightarrow P_2}(t) = 100 \frac{[\rho_{P_1}(t, T, P_2) - \rho^{qEOS}(T, P_2)]}{[\rho_{P_1}(t = 0, T, P_2) - \rho^{qEOS}(T, P_2)]}, \quad (1)$$

where $\rho_{P_1}(t, T, P_2)$ denotes the density of the structure obtained at the pressure P_1 and at time t after the pressure was reduced to the value P_2. According to this definition, the excess density of 100% indicates that the density did not relax and it is equal to the original density of the structure at pressure P_1, whereas 0% means that it is fully relaxed to the qEOS density under the new pressure value.

For quantitative description of the density relaxation process, we fit the time evolution of the excess density as

$$\delta\rho_{P_1 \rightarrow P_2}(T) = A + Be^{-t/\tau}, \quad (2)$$

where τ is the relaxation time of the structure.

The results in Fig. 3 show the temporal evolution of the density relaxation process in the a-SiO$_2$ (WS) and a-Si$_3$N$_4$ structures at different temperatures, while the pressure in the system was changed from $P_1 \rightarrow P_2$.

We see that the structure relaxes within a few ps at high ambient temperatures (see curves 7 → 3 GPa, 4500 K in the top graphs, and 10 → 5 GPa, 3300 K in the bottom graphs of Fig. 3), while the cooler ambient temperatures increase the relaxation times by an order of magnitude, at least. Moreover, we see that both structures fully relax only at high temperatures.

The complete pressure relaxation in a-SiO$_2$ (2 GPa → 0 GPa) and in a-Si$_3$N$_4$ (5 GPa → 0 GPa) at temperatures below the melting point (1500 K and 1650 K, respectively) did not result in the full recovery of the densities. We note that we observe this behavior in a-SiO$_2$ already near the melting point ($T = 3000$ K). In that simulation, the density was not able to reach the qEOS value at 0 GPa even after 1 ns of simulated time.
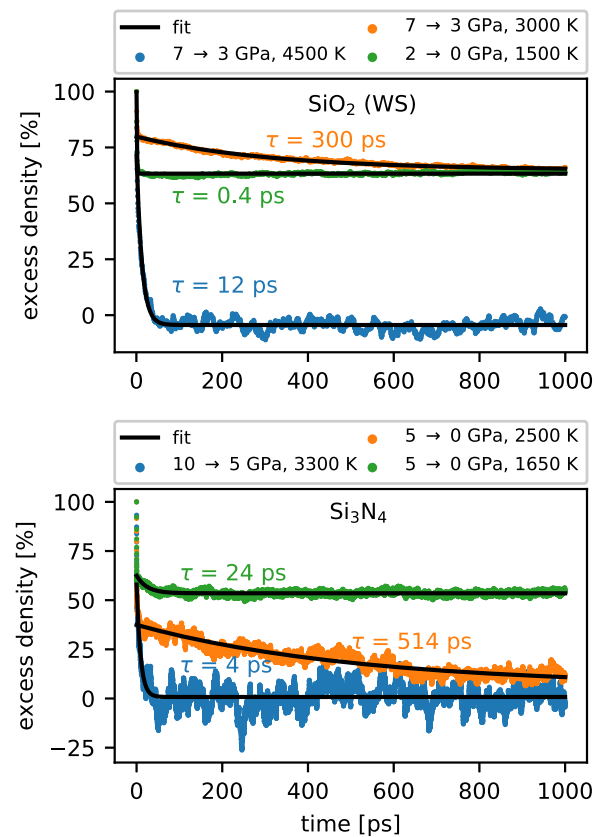

FIG. 3. Density relaxation of amorphous structures with time after a change in pressure. The y axis shows the excess density in the structure calculated according to Eq. (1). The top and bottom subfigures show the density relaxation for a-SiO$_2$ (WS) and a-Si$_3$N$_4$ structures, respectively. The black lines indicate the fit of the data with an exponential decay function from Eq. (2).

As we see in Fig. 3, the excess density in the simulations at lower ambient temperatures remained at the level >50% of its original value. This clearly indicates that compactified under pressure undercooled liquid phase is able to remain densified even after the pressure is fully removed. These results are in line with previous experiments, which showed the compaction of glass melts at high pressures [13,14,46]. The compactification of the melt under external pressure is not the same as the densification of a-SiO$_2$ upon melting [52], which was reported to recover slowly with time [53,54]. This ability to stabilize the compactified phase under external pressure may also explain the fact that track shell structure remains overdensified long after the impact.

C. Effect of pressure on density inside the track

The results presented in Figs. 1 and 2 suggest that the permanent densification of the track shell in a-SiO$_2$ and a-Si$_3$N$_4$ can be caused by the pressure sustained during the solidification stage of track formation, and that the presence of ion-induced point defects is not required to produce this effect. To verify this observation, we return to the interpolation scheme used in Fig. 3 and compare the density inside the track with the values $\rho^{qEOS}(T, P)$ interpolated from the heating curves in Fig. 2.
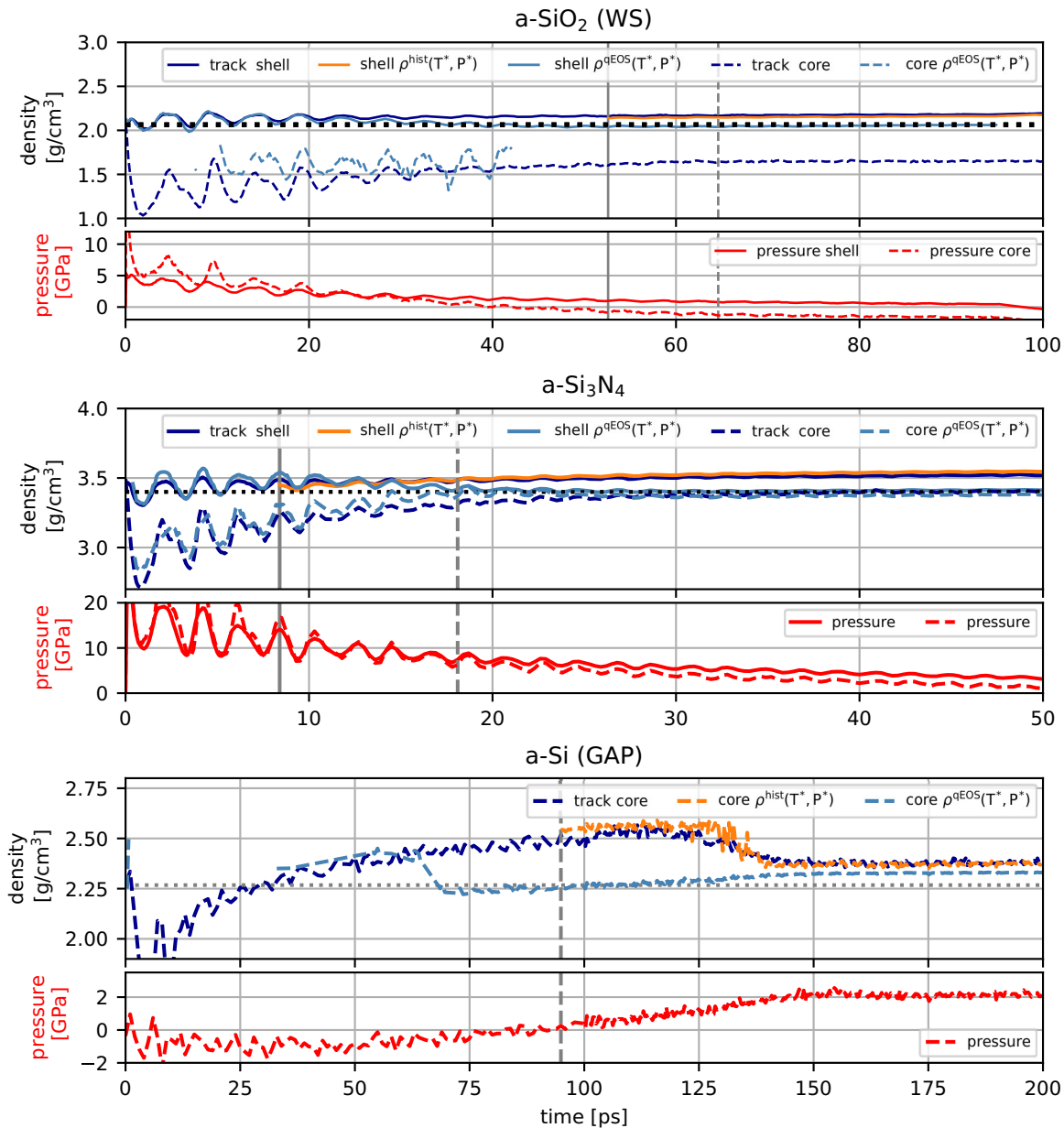
FIG. 4. Time evolution of the density and pressure inside the track in a-SiO$_2$ with Watanabe-Samela potential (top), a-Si$_3$N$_4$ and a-Si with GAP potential. The solid lines denote the track shell and the dashed ones the core; we show the actual simulation density, as well as the qEOS $\rho^{\mathrm{qEOS}}(T^*, P^*)$ prediction. We also include the density $\rho^{\mathrm{hist}}(T^*, P^*)$ for an amorphous structure cooled at the corresponding solidification pressure of each material according to Eq. (3). The original density in the cell is indicated with a black horizontal dashed line.

In Fig. 4, we show the temporal evolution of the density (dark blue line) and pressure (red line) in the track core region (within 1 nm radius from the center of the track) and shell (between 4–5 and 3–4 nm from the center for a-SiO$_2$ and a-Si$_3$N$_4$, respectively) as obtained in the simulations of SHI impacts. In the same graph, we include the density of structures (light blue line) obtained in the quasiequilibrium simulations $\rho^{q\mathrm{EOS}}(P^*, T^*)$ at the same temperature and pressure as T^* and P^* estimated inside the track. Asterisks mark the values averaged within the small regions of track structures in the MD simulation cell, as described in Sec. II.

Density oscillations shown in dark blue in Fig. 4 in both the core (dashed line) and the shell (solid line) regions of the track are coherent with the pressure fluctuations in the correspond-

ing regions (red dashed and solid curves, respectively). These present the thermoelastic wave generated in the matrix by the localized energy deposition along the ion path. Although the generated wave would in reality mainly propagate further, in the finite size MD simulation cell the wave returns via periodic boundaries. This artifact does not, however, affect the final density distribution in the corresponding regions, which we verified by changing the size of the cell (see Supplemental Material [42] for more details).

In Fig. 4 we see that the qEOS density curve interpolated for T^* and P^* found in the shell region (solid light blue curve) follows closely the curve of the shell density almost from the moment of the impact ($\leqslant 1$ ps), i.e., when the material around the ion path becomes molten.

We notice that both density curves in the track shell region, the actual and the qEOS-interpolated, start diverging after a certain time in all materials. We identify the point of divergence as the instant when the molten material starts solidifying and the viscosity increases. The solidification is initiated in each material under different pressures P_{sol}, which are ~2 GPa and ~8 GPa in a-SiO$_2$ and a-Si$_3$N$_4$, respectively. In a-Si, however, we see that track and qEOS curves start diverging earlier and both curves show a phase transition from HDL to LDL at different times as a consequence of the overheating effect seen in Fig. 2. From the sharp drop of the track density for a-Si in Fig. 4, we estimate that the solidification takes place approximately at 1 GPa in our simulations.

Although the temperature at this moment is still above the melting point in the corresponding potential (vertical solid gray line), the solidification of the structure has already begun. As we saw in Figs. 2 and 3, these materials exhibit a memory effect, i.e., when they solidify under pressure, they undergo structural modifications, which remain intact even after the pressure is released. The qEOS curve, however, is reconstructed from the quasiequilibrium densities at the given P^* and T^*. Therefore, it assumes instantaneous density relaxation to a metastable equilibrium density for the given condition without taking into account the history of the cooling condition.

As we saw in Fig. 3, this history is particularly important when structure cools under different pressure conditions. Hence, we have to take into account that in the region around the ion track, considering that the track shell in a-SiO$_2$ and a-Si$_3$N$_4$, or track core in a-Si, solidify at elevated pressures. In order to verify whether the compactification in the track regions indeed occurs due to solidification under high pressures, we take into consideration the cooling history of the amorphous structure in the track when modeling the density in the shell $\rho^{hist}(T^*, P^*)$ (orange solid line in Fig. 4). This density curve corresponds to the structure solidified at ambient pressure P_{sol} and whose network configuration remains unchanged after solidification despite changes of pressure.

To obtain $\rho^{hist}(T^*, P^*)$, we use the cooling curves $\rho^{cool}_{P_{sol}}(T^*)$ from Fig. 2, and include a compression related correction as follows:

$$\rho^{hist}(T^*, P^*) = \rho^{cool}_{P_{sol}}(T^*) \times e^{-K_{P_{sol}}(P^* - P_{sol})}, \qquad (3)$$

where $K_{P_{sol}}$ is the bulk modulus of that structure measured at 300 K. The results of this model are shown in Fig. 4 (orange line) for the shell after it started solidifying, i.e., after the temperature drops below the melting point.

We define the solidification pressure P_{sol} as the pressure at the moment when the curves describing the track-shell density and the quasiequilibrium density $\rho^{qEOS}(P^*, T^*)$ start deviating from one another in Fig. 4. As we discussed earlier, we estimate this pressure as 2, 8 and 1 GPa for a-SiO$_2$, a-Si$_3$N$_4$, and a-Si, respectively.

In Fig. 4, we see that the simple expression (3) is capable of capturing the density transformation in the track shells of a-SiO$_2$ and a-Si$_3$N$_4$, and in the track core of a-Si, and predicts similar compactification of the structure. The good agreement, hence, supports the original hypothesis that the overdense shell forms as a result of the liquid-to-solid phase transition under the elevated pressures caused by strong thermal expansion after the localized energy deposition.

In the simulations with a-Si, we see that the density in the core, at first, dropped below the initial density due to the initial thermal expansion, but then rapidly recovered and even increased to up to 3%. Unlike a-SiO$_2$ and a-Si$_3$N$_4$, the density in the core of a-Si remains low only for a short time (see Fig. 1), partially due to the large density increase in the LDL to HDL phase transition as well as due to the lower temperatures reached as a result of the higher thermal conductivity. The changes in density inside the track go hand-in-hand with the variations in pressure, which reaches up to 2 GPa at 200 ps after the ion impact. The results of the cooling curves in Fig. 2 confirm that the structure does not recover fully to the initial value if the solidification has happened under pressure. In that figure we see a ~2% increase in density upon cooling from the melt at 1 GPa.

The dynamics of density changes in this material is mainly explained by the phase transition from solid-to-LDL, and then the LDL-to-HDL transition. Without additional pressure the cooling would induce the reverse transitions, which we observe in Fig. 2 and the density fully recovers. Nevertheless, we observe a hysteresis with the fast cooling rate, similar to the one inside the ion track, due to the slower transition from HDL to LDL phase. This hysteresis is seen in Figs. 4 and 1, as the materials remain in the HDL phase at temperatures below the melting point, and leads to an earlier divergence between the $\rho^{qEOS}(T^*, P^*)$ and the track core density. Moreover, in Fig. 2 we notice that the hysteresis becomes yet more pronounced at higher pressures.

During the solidification of the shell, the track core is yet in the denser HDL phase and the pressures are negative or close to zero. These conditions allow the track shell to transition from HDL to the LDL. As this transition takes place, the shell takes more volume and the pressure inside the track rises. By the time the material within the core undergoes the phase transition into LDL, the pressure is high, and the LDL phase solidifies under pressure yielding a denser structure. The pressure inside the track remains high even after the ion track had cooled down. Despite this, the difference in Fig. 4 between $\rho^{qEOS}(T^*, P^*)$ and $\rho^{hist}(T^*, P^*)$ [see Eq. (3)] shows that about one-third of the densification in the track core is due to structural changes; therefore we expect this density increase to remain even if the stresses inside the core eventually fully relax.

The density of the track core in a-SiO$_2$, (dark blue dashed line), on the other hand, is considerably lower than that predicted by the qEOS model (light blue dashed line). We note that the pressure inside the track core during solidification is low (see red dashed line in Fig. 4). In the qEOS simulations, we see that at zero pressure the structure quenches into a solid resulting in a density lower than the initial one. The faster the cooling rate, the lower the final density becomes (compare the dotted and dot-dashed orange lines in top left panel of Fig. 2). Moreover in this region, the solidification happens under negative pressure, since the overdense track shell solidifies earlier giving rise to tensile stress in the track core.

We note, however, that the other a-Si potentials used in the current study, Tersoff and Stillinger-Weber, did not exhibit
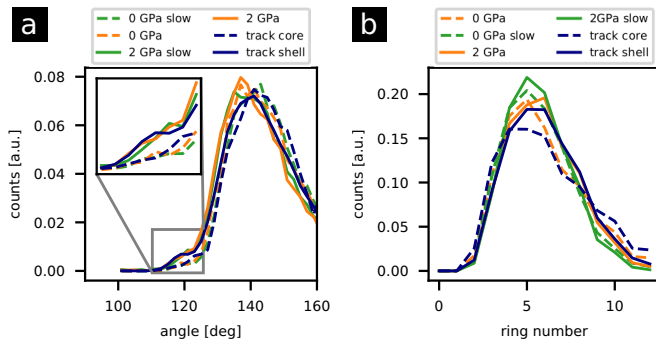
FIG. 5. Analysis of the a-SiO$_2$ structure in the core and shell regions of the track. We include as reference the analogous analysis for amorphous structures quenched at 0 and 2 GPa pressures. The subfigures include the following analysis: (a) Distribution of the Si-O-Si bond angles. (b) Ring distribution of the amorphous structure.

the same behavior of a-Si as we observed with the GAP. In these potentials, the pressures inside the track are very low and the overdense core forms due to the HDL phase, which is not capable to relax fully into LDL during the fast quench. Nevertheless, we believe that the interatomic forces are more accurately described in GAP, since the potential was fitted consistently to the DFT data; hence, we expect that this potential predicts more accurately the physics of the ultrafast phase transitions, which take place during the development of ion tracks in a-Si.

D. Ring and bond angle analysis

Previous computational studies identified specific changes in ring [13] and bond angle distributions [14] in pressure-induced densified a-SiO$_2$ structures. Hence, we further analyze the structure inside the track region in a-SiO$_2$ using the same approach to corroborate the finding that the structural changes in this region are pressure induced. In Fig. 5, we show the ring and the Si-O-Si bond angle distributions in the core and shell regions of the track. We included the same analysis for the smaller cells from Fig. 2 that are cooled under 0 and 2 GPa pressures. As we see in Fig. 2, the cooling rate did not affect significantly the density at high pressures, nevertheless, it might still modify other structural properties, apart from the density only. Therefore, we include the analysis for the smaller cells quenched at 0.02 K/fs and 0.002 K/fs cooling rates.

We observe in Fig. 5(a) a slight shift of the angle distribution towards the smaller bond angles and a noticeable increase in the low angle tail (less than 120 degrees) compared to the track core. We observe identical trend in the small cells, where the structures cooled under 2 GPa exhibit a small peak in the low bond-angle tail, which is missing in the structures cooled under 0 GPa. There is an insignificant difference in the distributions plotted for the structures cooled down with different cooling rates. The slower cooling rate resulted in a tiny shift of the main peak of the towards the larger angles. These trends has been observed previously with other interatomic potentials [52,55,56].

In Fig. 5(b) we show the analysis of the ring distribution for different structures. We see that the distribution in the track core is narrower than in the shell and shows larger fraction of the small rings. The small cells cooled under pressure show similar behavior and the distribution of the structures cooled with the rate 0.02 K/fs at 0 and 2 GPa resemble closely the distribution in the track core and shell, respectively. The structures cooled with the slower cooling rate 0.002 K/fs, however, show an increase of five- and six-member rings, and show less dependence on the applied pressure.

From the analysis of the ring and bond angle distributions, we can conclude that the structural changes seen inside the track originate from the transient pressure during the track cool down, as we have initially proposed. The analysis of the ring and bond angle distributions are consistent with our initial hypothesis, which attributed the structural changes inside the track to the transient pressure during the track cool down.

E. Formation mechanism of ion tracks in amorphous materials based on tetrahedral network

In Fig. 6, we summarize the presented results and illustrate with schematics of the formation mechanism of the ion track core-shell structure in the studied amorphous materials. The high pressures during the liquid-solid phase transition in the shell (or core in a-Si) region causes compactification of the amorphous structure, while the low pressure and fast quench rates in the core (or shell in a-Si) lead to formation of underdensified structure.

In this work, we addressed only the processes that develop within the time scales covered by the MD time scale. Hence, we are able to capture the ultrafast (subnanosecond) phase transitions that take place in the materials during the evolution of an ion track. While further relaxation of stresses frozen in the formed tracks via longer-term processes is possible, previous experiments on continuous permanent densification in a-SiO$_2$ during solidification under pressure [13,46] suggest that such relaxation will not be significant. To our knowledge, similar densification under pressure has not been yet reported in a-Si$_3$N$_4$ and a-Si despite the fact that the tetrahedral network is specific to the structure of these materials as well. Moreover, experimentally observed and confirmed in atomistic simulations core-shell (core) structures in a-Si$_3$N$_4$ (a-Si) [3,6], suggest that the compactified phase in the track remains stable because of extremely fast quench rate during the ion impact. Such fast quench rates are not accessible in macroscopic experiments. Moreover, the cylindrical symmetry of the track might also hinder the relaxation of the modified amorphous structure. The core-shell fine structure has not been observed in other amorphous materials, therefore, we attribute the formation of these fine structures in the studied materials to the remarkable stability of different tetrahedral network configurations typical to polyamorphic materials.

IV. CONCLUSION

In conclusion, we show that the core-shell (core) structures of the ion tracks develop in a-SiO$_2$/a-Si$_3$N$_4$ (a-Si) upon solidification of the amorphous network at different pressures:
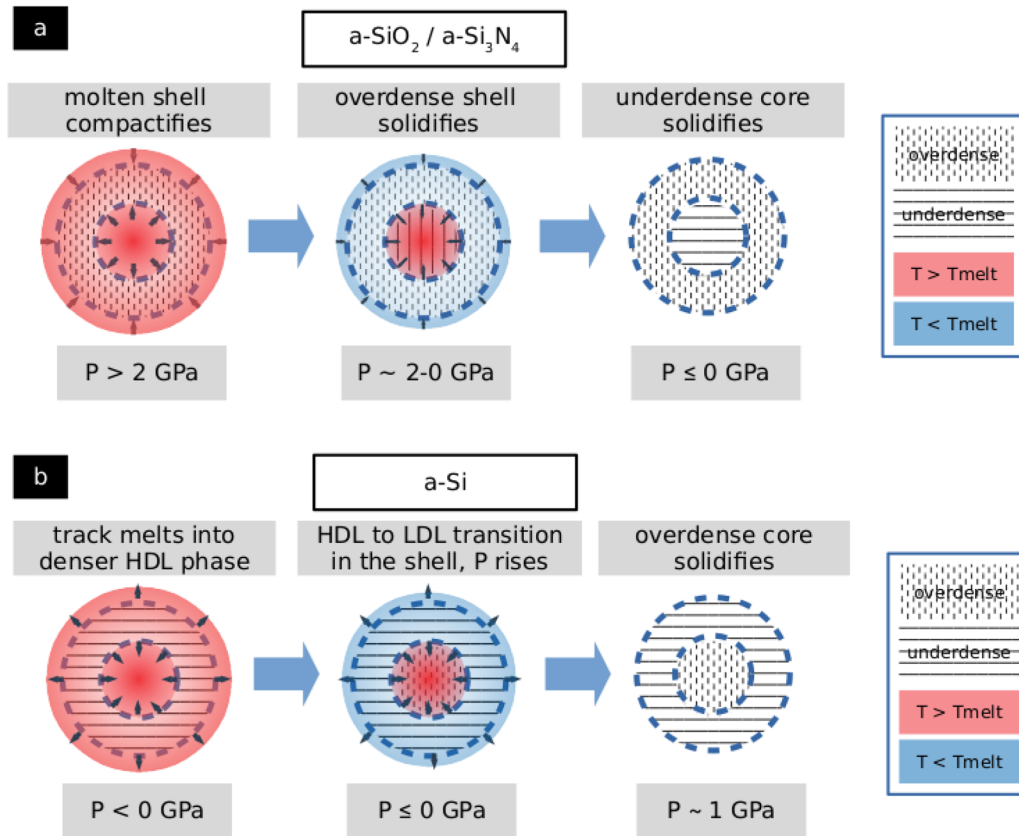
FIG. 6. Illustration of mechanisms leading to formation of the fine structure inside the track. The subfigures correspond to different amorphous materials: (a) for a-SiO$_2$ and a-Si$_3$N$_4$, (b) for a-Si.

overdense shell (elevated pressures), underdense core (low or negative pressures). The good agreement between the densification in the track and the equilibrium densities reached for corresponding structures in the same thermodynamic condition, shows that the densification in the shell region is not formed by the flow of defects into the cold surrounding matrix, as previously proposed, but due to compactification and solidification of the network under elevated pressures. Irradiation experiments show that the density modifications inside the track are stable at room temperature; we link the formation of these structures and their long lifetimes in the track to the polyamorphic nature of the tetrahedral networks, which exhibit multiple metastable configurations under pressure. These results clearly show that not only the temperature, but also the transient pressure due to an ion impact can lead to permanent structural modifications in the track.

[1] P. Kluth, C. S. Schnohr, O. H. Pakarinen, F. Djurabekova, D. J. Sprouster, R. Giulian, M. C. Ridgway, A. P. Byrne, C. Trautmann, D. J. Cookson, K. Nordlund, and M. Toulemonde, Fine Structure in Swift Heavy Ion Tracks in Amorphous SiO$_2$, Phys. Rev. Lett. **101**, 175503 (2008).

[2] P. Kluth, O. H. Pakarinen, F. Djurabekova, R. Giulian, M. C. Ridgway, A. Byrne, and K. Nordlund, Nanoscale density fluctuations in swift heavy ion irradiated amorphous sio2, J. Appl. Phys. **110**, 123520 (2011).

[3] P. Mota-Santiago, H. Vazquez, T. Bierschenk, F. Kremer, A. Nadzri, D. Schauries, F. Djurabekova, K. Nordlund, C. Trautmann, S. Mudie *et al.*, Nanoscale density variations induced by high energy heavy ions in amorphous silicon nitride and silicon dioxide, Nanotechnology **29**, 144004 (2018).

[4] O. H. Pakarinen, F. Djurabekova, K. Nordlund, P. Kluth, and M. C. Ridgway, Molecular dynamics simulations of the structure of latent tracks in quartz and amorphous sio2, Nucl. Instrum. Meth. Phys. Res. B **267**, 1456 (2009).

[5] A. Rivera, J. Olivares, A. Prada, M. L. Crespillo, M. J. Caturla, E. M. Bringa, J. M. Perlado, and O. Peña-Rodríguez, Permanent modifications in silica produced by ion-induced high electronic excitation: Experiments and atomistic simulations, Sci. Rep. **7**, 1 (2017).

[6] T. Bierschenk, R. Giulian, B. Afra, M. D. Rodriguez, D. Schauries, S. Mudie, O. H. Pakarinen, F. Djurabekova, K. Nordlund, O. Osmani *et al.*, Latent ion tracks in amorphous silicon, Phys. Rev. B **88**, 174111 (2013).

[7] K. Kupka, A. Leino, W. Ren, H. Vázquez, E. Åhlgren, K. Nordlund, M. Tomut, C. Trautmann, P. Kluth, and M. Toulemonde *et al.*, Graphitization of amorphous carbon by swift heavy ion impacts: Molecular dynamics simulation, Diam. Relat. Mater. **83**, 134 (2018).

[8] M.-d. Hou, S. Klaumünzer, and G. Schumacher, Dimensional changes of metallic glasses during bombardment with fast heavy ions, Phys. Rev. B **41**, 1144 (1990).

[9] M. Rodriguez, B. Afra, C. Trautmann, M. Toulemonde, T. Bierschenk, J. Leslie, R. Giulian, N. Kirby, and P. Kluth, Morphology of swift heavy ion tracks in metallic glasses, J. Non-Cryst. Solids **358**, 571 (2012).

[10] V. Borodin, A. Volkov, and D. Korolev, Viscous flow of amorphous metals in swift heavy ion tracks, Nucl. Instrum. Meth. Phys. Res. B **209**, 122 (2003).

[11] A. Benyagoub, S. Klaumünzer, and M. Toulemonde, Radiation-induced compaction and plastic flow of vitreous silica, Nucl. Instrum. Meth. Phys. Res. B **146**, 449 (1998).

[12] T. Loerting, V. V. Brazhkin, and T. Morishita, Multiple amorphous-amorphous transitions, *Advances in Chemical Physics* (John Wiley & Sons, Ltd, 2009), pp. 29–82.

[13] K. Trachenko and M. T. Dove, Compressibility, kinetics, and phase transition in pressurized amorphous silica, Phys. Rev. B **67**, 064107 (2003).

[14] Y. Wang, T. Sakamaki, L. B. Skinner, Z. Jing, T. Yu, Y. Kono, C. Park, G. Shen, M. L. Rivers, and S. R. Sutton, Atomistic insight into viscosity and density of silicate melts under pressure, Nature Commun. **5**, 3241 (2014).

[15] S. Sastry and C. A. Angell, Liquid–liquid phase transition in supercooled silicon, Nature Mater. **2**, 739 (2003).

[16] N. Jakse and A. Pasturel, Liquid-Liquid Phase Transformation in Silicon: Evidence from First-Principles Molecular Dynamics Simulations, Phys. Rev. Lett. **99**, 205702 (2007).

[17] M. Beye, F. Sorgenfrei, W. F. Schlotter, W. Wurth, and A. Föhlisch, The liquid-liquid phase transition in silicon revealed by snapshots of valence electrons, Proc. Natl. Acad. Sci. **107**, 16772 (2010).

[18] S. Munetoh, T. Motooka, K. Moriguchi, and A. Shintani, Interatomic potential for si–o systems using tersoff parameterization, Comput. Mater. Sci. **39**, 334 (2007).

[19] J. Samela, K. Nordlund, V. N. Popok, and E. E. B. Campbell, Origin of complex impact craters on native oxide coated silicon surfaces, Phys. Rev. B **77**, 075309 (2008).

[20] F. de Brito Mota, J. F. Justo, and A. Fazzio, Structural properties of amorphous silicon nitride, Phys. Rev. B **58**, 8323 (1998).

[21] J. Tersoff, Empirical interatomic potential for silicon with improved elastic properties, Phys. Rev. B **38**, 9902 (1988).

[22] F. H. Stillinger and T. A. Weber, Computer simulation of local order in condensed phases of silicon, Phys. Rev. B **31**, 5262 (1985).

[23] A. P. Bartók, J. Kermode, N. Bernstein, and G. Csányi, Machine Learning a General-Purpose Interatomic Potential for Silicon, Phys. Rev. X **8**, 041048 (2018).

[24] V. L. Deringer, N. Bernstein, A. P. Bartók, M. J. Cliffe, R. N. Kerber, L. E. Marbella, C. P. Grey, S. R. Elliott, and G.

Csányi, Realistic atomistic structure of amorphous silicon from machine-learning-driven molecular dynamics, J. Phys. Chem. Lett. **9**, 2879 (2018).

[25] P. C. Kelires and J. Tersoff, Glassy Quasithermal Distribution of Local Geometries and Defects in Quenched Amorphous Silicon, Phys. Rev. Lett. **61**, 562 (1988).

[26] M. D. Kluge, J. R. Ray, and A. Rahman, Amorphous-silicon formation by rapid quenching: A molecular-dynamics study, Phys. Rev. B **36**, 4234 (1987).

[27] Y. H. Lee, R. Biswas, C. M. Soukoulis, C. Z. Wang, C. T. Chan, and K. M. Ho, Molecular-dynamics simulation of thermal conductivity in amorphous silicon, Phys. Rev. B **43**, 6573 (1991).

[28] M. Backman, F. Djurabekova, O. H. Pakarinen, K. Nordlund, Y. Zhang, M. Toulemonde, and W. J. Weber, Cooperative effect of electronic and nuclear stopping on ion irradiation damage in silica, J. Phys. D **45**, 505305 (2012).

[29] A. A. Leino, O. Pakarinen, F. Djurabekova, K. Nordlund, P. Kluth, and M. C. Ridgway, Swift heavy ion shape transformation of au nanocrystals mediated by molten material flow and recrystallization, Mater. Res. Lett. **2**, 37 (2014).

[30] A. Leino, S. Daraszewicz, O. H. Pakarinen, K. Nordlund, and F. Djurabekova, Atomistic two-temperature modelling of ion track formation in silicon dioxide, Europhys. Lett. **110**, 16004 (2015).

[31] A. A. Leino, S. L. Daraszewicz, O. H. Pakarinen, F. Djurabekova, K. Nordlund, B. Afra, and P. Kluth, Structural analysis of simulated swift heavy ion tracks in quartz, Nucl. Instrum. Meth. Phys. Res. B **326**, 289 (2014).

[32] J. Zhen, Q. Yang, Y. Yan, X. Jiang, S. Yan, W. Chen, and X. Guo, Molecular dynamics study of structural damage in amorphous silica induced by swift heavy-ion radiation, Radiat. Eff. Defects Solids **171**, 340 (2016).

[33] W. Li, X. Wang, X. Zhang, S. Zhao, H. Duan, and J. Xue, Mechanism of the defect formation in supported graphene by energetic heavy ion irradiation: The substrate effect, Sci. Rep. **5**, 9935 (2015).

[34] T. Björkman, S. Kurasch, O. Lehtinen, J. Kotakoski, O. V. Yazyev, A. Srivastava, V. Skakalova, J. H. Smet, U. Kaiser, and A. V. Krasheninnikov, Defects in bilayer silica and graphene: Common trends in diverse hexagonal two-dimensional systems, Sci. Rep. **3**, 3482 (2013).

[35] A. Hamedani, J. Byggmästar, F. Djurabekova, G. Alahyarizadeh, R. Ghaderi, A. Minuchehr, and K. Nordlund, Insights into the primary radiation damage of silicon by a machine learning interatomic potential, Mater. Res. Lett. **8**, 364 (2020).

[36] K. Nordlund and R. S. Averback, Atomic displacement processes in irradiated amorphous and crystalline silicon, Appl. Phys. Lett. **70**, 3101 (1997).

[37] K. M. Beardmore and N. Grønbech-Jensen, Direct simulation of ion-beam-induced stressing and amorphization of silicon, Phys. Rev. B **60**, 12610 (1999).

[38] K. Nordlund, 2010, PARCAS computer code. The main principles of the molecular dynamics algorithms are presented in Refs. [57,58]. The adaptive time step and electronic stopping algorithms are the same as in Ref. [59].

[39] S. Plimpton, Fast parallel algorithms for short-range molecular dynamics, Tech. Rep. (Sandia National Labs, Albuquerque, 1993).

[40] F. Wooten, K. Winer, and D. Weaire, Computer Generation of Structural Models of Amorphous Si and Ge, Phys. Rev. Lett. **54**, 1392 (1985).

[41] F. Djurabekova and K. Nordlund, Atomistic simulation of the interface structure of si nanocrystals embedded in amorphous silica, Phys. Rev. B **77**, 115325 (2008).

[42] See Supplemental Material at http://link.aps.org/supplemental/10.1103/PhysRevMaterials.5.065603 for additional information regarding the simulations performed in this manuscript.

[43] I. Lifshits, M. Kaganov, and L. Tanatarov, On the theory of radiation-induced changes in metals, J. Nucl. Energy, Part A **12**, 69 (1960).

[44] M. Waligorski, R. Hamm, and R. Katz, *The Radial Distribution of Dose Around the Path of a Heavy Ion in Liquid Water* (University of Nebraska, Lincoln, 1986).

[45] M. C. Ridgway, T. Bierschenk, R. Giulian, B. Afra, M. D. Rodriguez, L. L. Araujo, A. P. Byrne, N. Kirby, O. H. Pakarinen, F. Djurabekova, K. Nordlund, M. Schleberger, O. Osmani, N. Medvedev, B. Rethfeld, and P. Kluth, Tracks and Voids in Amorphous Ge Induced by Swift Heavy-Ion Irradiation, Phys. Rev. Lett. **110**, 245502 (2013).

[46] R. Brueckner, Properties and structure of vitreous silica. I, J. Non-Cryst. Solids **5**, 123 (1970).

[47] G. Bartenev and N. Scheglova, High-temperature relaxation mechanisms in inorganic glasses, J. Non-Cryst. Solids **37**, 285 (1980).

[48] Y. Morita, K. Nakajima, M. Suzuki, K. Narumi, Y. Saitoh, N. Ishikawa, K. Hojou, M. Tsujimoto, S. Isoda, and K. Kimura, Surface effect on ion track formation in amorphous si3n4 films, Nucl. Instrum. Meth. Phys. Res. B **315**, 142 (2013).

[49] H. J. Berendsen, J. v. Postma, W. F. van Gunsteren, A. DiNola, and J. R. Haak, Molecular dynamics with coupling to an external bath, J. Chem. Phys. **81**, 3684 (1984).

[50] W. G. Hoover and B. L. Holian, Kinetic moments method for the canonical ensemble distribution, Phys. Lett. A **211**, 253 (1996).

[51] K. Vollmayr, W. Kob, and K. Binder, Cooling-rate effects in amorphous silica: A computer-simulation study, Phys. Rev. B **54**, 15808 (1996).

[52] J. M. D. Lane, Cooling rate and stress relaxation in silica melts and glasses via microsecond molecular dynamics, Phys. Rev. E **92**, 012320 (2015).

[53] J. Mackenzie, High-pressure effects on oxide glasses: I, densification in rigid state, J. Am. Ceram. Soc. **46**, 461 (1963).

[54] M. Kanzaki, Melting of silica up to 7 gpa, J. Am. Ceram. Soc. **73**, 3706 (1990).

[55] X. Li, W. Song, K. Yang, N. A. Krishnan, B. Wang, M. M. Smedskjaer, J. C. Mauro, G. Sant, M. Balonis, and M. Bauchy, Cooling rate effects in sodium silicate glasses: Bridging the gap between molecular dynamics simulations and experiments, J. Chem. Phys. **147**, 074501 (2017).

[56] W. Jin, R. K. Kalia, P. Vashishta, and J. P. Rino, Structural Transformation, Intermediate-Range Order, and Dynamical behavior of SiO 2 Glass at High Pressures, Phys. Rev. Lett. **71**, 3146 (1993).

[57] K. Nordlund, M. Ghaly, R. S. Averback, M. Caturla, T. Diaz de la Rubia, and J. Tarus, Defect production in collision cascades in elemental semiconductors and fcc metals, Phys. Rev. B **57**, 7556 (1998).

[58] M. Ghaly, K. Nordlund, and R. S. Averback, Molecular dynamics investigations of surface damage produced by kilo-electronvolt self-bombardment of solids, Philos. Mag. A **79**, 795 (1999).

[59] K. Nordlund, Molecular dynamics simulation of ion ranges in the 1–100 kev energy range, Comput. Mater. Sci. **3**, 448 (1995).